

Article

Shell-like ZnO–Graphene/Epoxy Coating with Outstanding Anticorrosion Performance and Weather Resistance

Yu Wang ^{1,†}, Lei Ma ^{2,†}, Yanan Niu ¹, Huachao Ma ¹, Yuguang Lv ^{1,2,*} and Kuilin Lv ^{3,*}

¹ College of Materials Science and Engineering, Jiamusi University, Jiamusi 154007, China; m18804686070@163.com (Y.W.); m18310045776@163.com (Y.N.); m18769082751@163.com (H.M.)

² College of Pharmacy, Jiamusi University, Jiamusi 154007, China; m13351653496@163.com

³ China Testing & Certification International Group Co., Ltd., Chaoyang District, Beijing 100024, China

* Correspondence: yuguanglv@163.com (Y.L.); lv_k_l@163.com (K.L.)

† These authors contributed equally to this work.

Abstract: Throughout millions of years of biological evolution, shell structures have developed a highly complex layered organic–inorganic structure that makes them effective against a wide range of external impacts, including mechanical stress and chemical corrosion. Therefore, shell-like biomimetic materials are considered to possess high strength and toughness. Nevertheless, although shell structures have exhibited superior performance across multiple domains, understanding of their structural complexities and corrosion protection mechanisms remains relatively limited within the scope of human knowledge. In this study, alternating ZnO–graphene/epoxy coatings featuring shell-like structures were synthesized, and their anticorrosion properties were evaluated through the incorporation of ZnO to enhance the dispersion of graphene. Electrochemical impedance spectroscopy (EIS) tests showed that with an increased number of ZnO–graphene layers, the coating resistance of the bionic composite coating also increased: from $8.21 \times 10^7 \Omega \cdot \text{cm}^2$ of the pure epoxy coating to $7.64 \times 10^8 \Omega \cdot \text{cm}^2$. The composite coating, comprising three alternating layers of zinc oxide and four layers of epoxy resin, exhibited an electrochemical impedance two orders of magnitude greater than that of pure epoxy resin following immersion in a 3.5% sodium chloride solution, demonstrating excellent corrosion resistance. The results showed that with increased ZnO–graphene layers, ZnO–graphene disperses more uniformly in water and has greater rigidity.



Academic Editor: Ioana Demetrescu

Received: 25 November 2024

Revised: 25 December 2024

Accepted: 3 January 2025

Published: 8 January 2025

Citation: Wang, Y.; Ma, L.; Niu, Y.; Ma, H.; Lv, Y.; Lv, K. Shell-like ZnO–Graphene/Epoxy Coating with Outstanding Anticorrosion Performance and Weather Resistance. *Coatings* **2025**, *15*, 63. <https://doi.org/10.3390/coatings15010063>

Copyright: © 2025 by the authors. Licensee MDPI, Basel, Switzerland. This article is an open access article distributed under the terms and conditions of the Creative Commons Attribution (CC BY) license (<https://creativecommons.org/licenses/by/4.0/>).

Keywords: biomimetic; shell-like structure; graphite; anticorrosion

1. Introduction

Corrosion is defined as the deterioration of metallic materials in an environment due to chemical reactions on the metal surface or interface, electrochemical processes, or physical actions. These actions may include the combined effects of mechanical and biological factors, ultimately leading to changes in the metal's properties and causing damage to the metal itself, the surrounding environment, or components of the technical systems they form. Corrosion annually results in substantial economic losses and extensive social impacts [1,2]. According to statistics, the direct economic loss caused by metal corrosion in China is about CNY 500 billion per year, accounting for about 6% of GDP. Currently, the primary methods for protecting metals encompass cathodic protection, corrosion-resistant materials, and surface coatings. Among these, the surface coating method stands out as a highly favored and cost-effective approach, due to its operational simplicity and superior protective attributes [3–6]. Recent studies have demonstrated

that incorporating anticorrosion fillers (such as glass flakes, mica sheets, graphite sheets, and zinc powder) into organic coating matrices not only fills the voids within the coating, thereby reducing the quantity of resin and solvent required, but also enhances the physical barrier properties, wear resistance, and mechanical strength of the coating. Graphene (Gr) is considered by researchers to be the most ideal nanofiller for organic protective coatings due to its extraordinarily large specific surface area ($2630 \text{ m}^2/\text{g}$), large aspect ratio, excellent hydrophobicity, lubricity, mechanical properties, and electrical and thermal conductivity [7]. Graphene is distributed in a random manner in polymer resins, giving organic coatings good surface hydrophobicity and physical barrier effects. The addition of only a small amount of graphene ($<0.5 \text{ wt.}\%$) can increase the coating impedance by more than 10 times, which is superior to other conventional fillers [8].

Graphene compound paint has the advantages of high-barrier, super-hydrophobic, chemically inert, and friction-resistant properties, and so on, which makes it possible to enhance the synthesis capability of the organic paint [9–16]. However, aggregation and galvanic corrosion are the main technical issues in the fabrication of graphene compound paint. Firstly, it is necessary to get rid of the aggregation of graphene, enhance the dispersity of the matrix, increase the interfacial compatibility between the lamellae and the resin matrix, and eliminate the galvanic corrosion effect, in order to achieve the coating's high reliability and long-lasting anticorrosion of the coating. Researchers have explored and developed many different methods to overcome the above bottlenecks, which mainly include surface modification [9–11], reduction in filler loading [12], and introduction of active additives (e.g., corrosion inhibitors [13], active metals [14], conductive polymers [15], and semiconducting materials [16], etc.). Lv et al. [17], by means of ball milling, achieved the diffusion of graphite in epoxy (EP) paint by controlling the size of nanoplates, thereby enhancing the anticorrosive properties of the epoxy. Du et al. [18] discovered that PANI is not only an outstanding disperser of graphene but also an effective anticorrosive agent that can be used to protect the surface of graphene. In addition, some semiconductor oxides can also passivate metal surfaces to provide additional protection to the substrate [19,20]. Wang Fuhui of the Shenyang Institute of Metals and his team have verified the synergy of $\text{Co}(\text{OH})_2$ with graphene [19].

The challenges of life in nature have driven many organisms to evolve remarkable impermeability and corrosion resistance, offering valuable insights for the structural design of new high-performance anticorrosion coatings [21–24]. A prime example is found in mollusks, whose hard shells enable them to endure mechanical impacts and corrosive environments [21]. The nacre layer of mollusk shells exemplifies a brick-and-mortar structure: aragonite platelets (“bricks”) are embedded within an organic matrix (“mortar”). The organic substrate functions as a lubricant, allowing neighboring “bricks” to slide and prevent excessive slippage between layers, much like glue. The exceptional mechanical properties, functional barriers, and ionic transport control that arise from the ordered interlayer structure and the abundant interfacial interactions within the pearl layer [25–27] provide valuable insights into the creation of high-performance 2D composite coatings. For instance, Lutkenhaus et al. [28] developed a highly oriented, aligned rGO–PVA structured coating by spraying a homogeneous mixture of graphene oxide (rGO) and poly(vinyl alcohol) (PVA), which effectively prevented the infiltration of corrosive media into the coating and significantly enhanced its physical barrier properties. Zhong Jing et al. [15] created a bionic compound coating with a $17 \text{ }\mu\text{m}$ -thick “anti-pearl” structure using the layer-by-layer technique based on GO and epoxy resin. This technique improved the coating's density and bolstered its barrier and mechanical performance.

In this study, we addressed the issue of graphite agglomeration by synthesizing ZnO-doped graphene (ZnO–Gr) powders with low defect edges by adding ZnO to graphite.

Subsequently, we crafted a biomimetic composite coating with a shell-like structure through the successive application of EP and ZnO–Gr coatings. This coating was named XZG-4EP (with X representing the number of ZnO–Gr layers, ranging from 1 to 3). The micro-molecular assembly of ZnO–Gr and EP was achieved via surface deposition, leading to the formation of a two-dimensional biomimetic composite coating with exceptional hardness and corrosion resistance. We explored the correlation between the microscopic arrangement and interfacial structure of the 2D materials and the corrosion resistance, as well as the mechanical properties of the composite coatings. The corrosion behavior of both the pure epoxy resin coating and the bionic composite coating on steel was examined using electrochemical and saltwater immersion tests. The findings indicated that the bionic coating exhibits significantly enhanced corrosion resistance compared to the pure epoxy resin coating.

2. Materials and Methods

2.1. Materials

The graphite was provided by Sigma-Aldrich Corporation (Shanghai, China). Nanometer zinc oxide (ZnO, AR) and sodium chloride (99.9%) were bought from Aladdin Holdings Group (Shanghai, China). The water-borne epoxide dispersion and co-solvent were bought from Shanghai Macklin Biochemical Company (Shanghai, China). The Q235 steel base plate (dimensions of 20 mm × 20 mm × 0.3 mm) was first ground using 150-, 300-, and 800-mesh sandpaper, followed by ultrasonic washing in ethanol and then drying at ambient temperature. None of the reagents was processed.

2.2. Characterization of Samples

The shape of the surface, the cross section, and the element distribution of the specimens were studied by SEM (SEM, S-4800, Hitachi, Tokyo, Japan). The thickness of the coating was tested using an ultra-depth field microscope (KEYENCE, Kansas City, MO, USA, VHX-970F). The XRD patterns were taken at a speed of 5°/min from 5° to 90° of the 2θ angle using an X-ray powder diffractometer with a characteristic wavelength (XRD Terra, Innov-X, Woburn, MA, USA). The function group and the crystalline structure of the composites were characterized by FTIR (FT-IR, Shimadzu IRPrestige-21, Kyoto, Japan). A contact angle gauge (OCAH200, Dataphysics, Filderstadt, Germany) was used to measure the static contact angle. The anticorrosion performance of the paint was assessed on a DH7000 electrochemistry station (Jiangsu Donghua Analytical Instrument Company, Taizhou, China). The porosity of the coating was tested by an RMCT-4000 high-resolution micro-CT detection system (Lima Precision Measuring Technology, Co., Ltd., Suzhou, China).

2.3. Synthesis of ZnO–Gr Composites

ZnO powder (200 mg) was accurately weighed, 20 mL of ethanol solution added, and then 20 mg of Gr powder added under continuous stirring for 30 min to make the mixture homogeneous, and then ultrasonic treatment was carried out for 2 h to obtain the ZnO–Gr dispersion. Finally, the dispersion was freeze-dried for 12 h to obtain ZnO–Gr.

2.4. Preparation of Anticorrosive Shell-like Coating XZG-4EP (X = 1, 2, 3)

EP and ZnO–Gr dispersions were alternately applied on a Q235 steel base plate, with EP as base and top layer. Firstly, EP was applied to the base material after being solidified for 12 h at ambient temperature. The ZnO–Gr dispersion was applied to the EP layer and solidified for 12 h at ambient temperature. The aforementioned procedures were iteratively executed to achieve ZnO–Gr layers of 1, 2, and 3 in the composite coatings, designated

XZG-4EP (where X = 1, 2, or 3). Additionally, for comparative analysis, four layers of pure epoxy coatings were applied and labeled 4EP.

2.5. Electrochemical Measurements

Electrochemistry impedance spectrometry (EIS) was performed on the DH7000 electrochemistry station with a typical 3-electrode system in 3.5 wt% NaCl artificially. The coated steels acted as working electrodes, the platinum plate was a counter electrode, and the saturated calomel electrode was a reference electrode. Before measurement, the sample was immersed in 3.5 wt% NaCl solution, and a Tafel polarization experiment was carried out based on the experimental results. The set rate was 2 mV S^{-1} . Based on the instrument measurement, the relationship between the corrosion potential (E_{corr}) and the corrosion current density (I_{corr}) was calculated. In order to guarantee the precision and reliability of EIS, three sets of parallel specimens were prepared and each set of experiments was repeated five times.

2.6. Coating Application Performance Test

2.6.1. Coating Porosity Measurement

X-ray computed tomography (X-CT) imaging technology enables non-destructive scanning of the micro-pore structure of composite materials, allowing for the analysis of porosity, distribution, and other parameters from X-CT images. In this study, RMCT-4000 equipment was utilized, and the X-CT scanning images were analyzed to determine the porosity of the cross section.

2.6.2. Coating Adhesion Test

The adhesion strength of coating samples was assessed utilizing the Positest AT-A automatic pull-off adhesion tester, produced by Delesko (Big Spring, TX, USA). Prior to testing, the surface of the coating and the test specimen (with a diameter of 20 mm) were roughened using 600-mesh sandpaper for proper bonding. The coating was then adhered to the test specimen with fast-setting AB adhesive and allowed to cure at room temperature for a period of 24 h. The adhesion tester measured the critical tensile force necessary to detach the coating from the steel substrate, which represented the adhesion force of the coating on the steel surface. For each component of the coating, five replicate samples were tested, and the results were averaged to ensure accuracy.

2.6.3. Hardness Test of Coated Pencils

Determination of hardness was conducted in accordance with GB/T6739-2006 [17]. The sample metal plate was placed on a horizontal surface, and the pencil was held horizontally, ensuring an angle of 45° between the faces. A straight line was then drawn away from the operator. Starting with the hardest pencil (6H), the hardness was gradually reduced (6H–6B) until the pencil no longer cut into the coating. The hardness of the coating was recorded as the hardness of the pencil at that point.

2.6.4. Impact Strength Test of Coating

In accordance with GB/T1732-1993 [17]—Method for Determining the Impact Resistance of Paint Films, a hammer weighing 1 kg was selected to conduct a 50 cm drop test on the coating. Subsequently, high-magnification observations were performed to assess whether the coating exhibited any cracking, wrinkling, or peeling.

3. Results and Discussion

3.1. Characterization of Samples and Coatings

3.1.1. Morphological Characterization of Samples and Coatings

Figure 1 shows the SEM images of Gr and ZnO–Gr. Graphene has a sheet-like structure with a flat and smooth surface with curved and wrinkled edges (Figure 1a,b). ZnO presented a petal-shaped spherical structure formed by interspersed nanosheets, with uniform size and morphology, the diameter of the nanospherical structure was about 4 μm , and the surface of the nanosheet layer was smooth (Figure 1b). As indicated by the results in Figure 1c,d, petal-like zinc oxide nanoparticles were dispersed on the graphene surface, forming a cross-linked network with the graphene. This interaction resulted in a roughened graphene surface, featuring numerous small protrusions and an increased plane roughness. These SEM images further corroborated the formation of the ZnO–Gr composite.

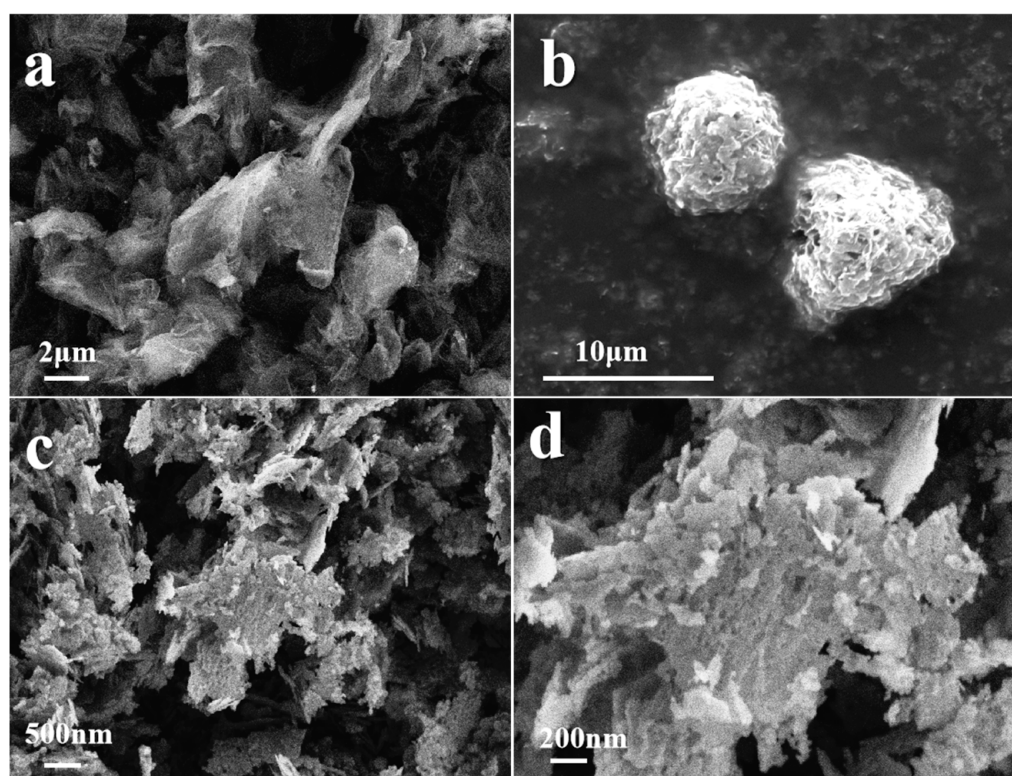


Figure 1. SEM of Gr (a), ZnO (b), and ZnO–Gr (c,d) samples.

To validate the multi-layered shell structure, SEM was used to obtain a cross section of the composite paint, and the EDS line scan method was used to obtain a cross section, which is illustrated in Figure 2. In Figure 2a, the pure epoxy resin paint exhibits a classic type of brittle crack with a characteristic slot shape and a flat crack face. The EDS line scan (Figure 2b) and the mapping (Figure 2c) reveal that the carbon (C) and oxygen (O) components are evenly distributed in the coating, which means that there is no delamination in the EP coating. After applying a layer of ZnO–Gr, the coating showed an obvious delamination structure (Figure 2d), and the EDS line scan results also proved that the Zn elements were distributed in the coating (Figure 2e). Through EDS mapping analysis (Figure 2f), it is evident that the C element is uniformly distributed in the coating, which proves that with the addition of ZnO, the dispersing ability of the graphite powder is improved and the graphite powder is uniformly dispersed. When the ZnO–Gr addition was increased to two layers, the cross-sectional view revealed a distinct lamellar structure, with the lamination of the shell-like configuration being further intensified (Figure 2g). The

results of the EDS line scanning of Zn also proved the separation between the bilayered ZnO–Gr coatings and epoxy coatings (Figure 2h), and the EDS mapping results further demonstrated the formation of the delamination structure and the role of ZnO in making the graphite powder uniformly dispersed in the coating (Figure 2i). When three layers of ZnO–Gr were coated, the cross section of the coating formed an obvious shell-like structure, and the emergence of the layered structure of one epoxy layer–ZnO–Gr coating can be seen very clearly (Figure 2j). The variations in the C, O, and Zn peaks observed in the EDS line-scanning results (Figure 2k) provide a clear indication of the coating's layered structure. In the EDS mapping result (Figure 2l), the Zn element is obviously distributed in the three-layer structure, while the C element is uniformly distributed in all layers, which further proves that the formation of the shell-like structure and the incorporation of ZnO enhance the dispersing ability of the graphite powder, which in turn improves the corrosion resistance of the coating.

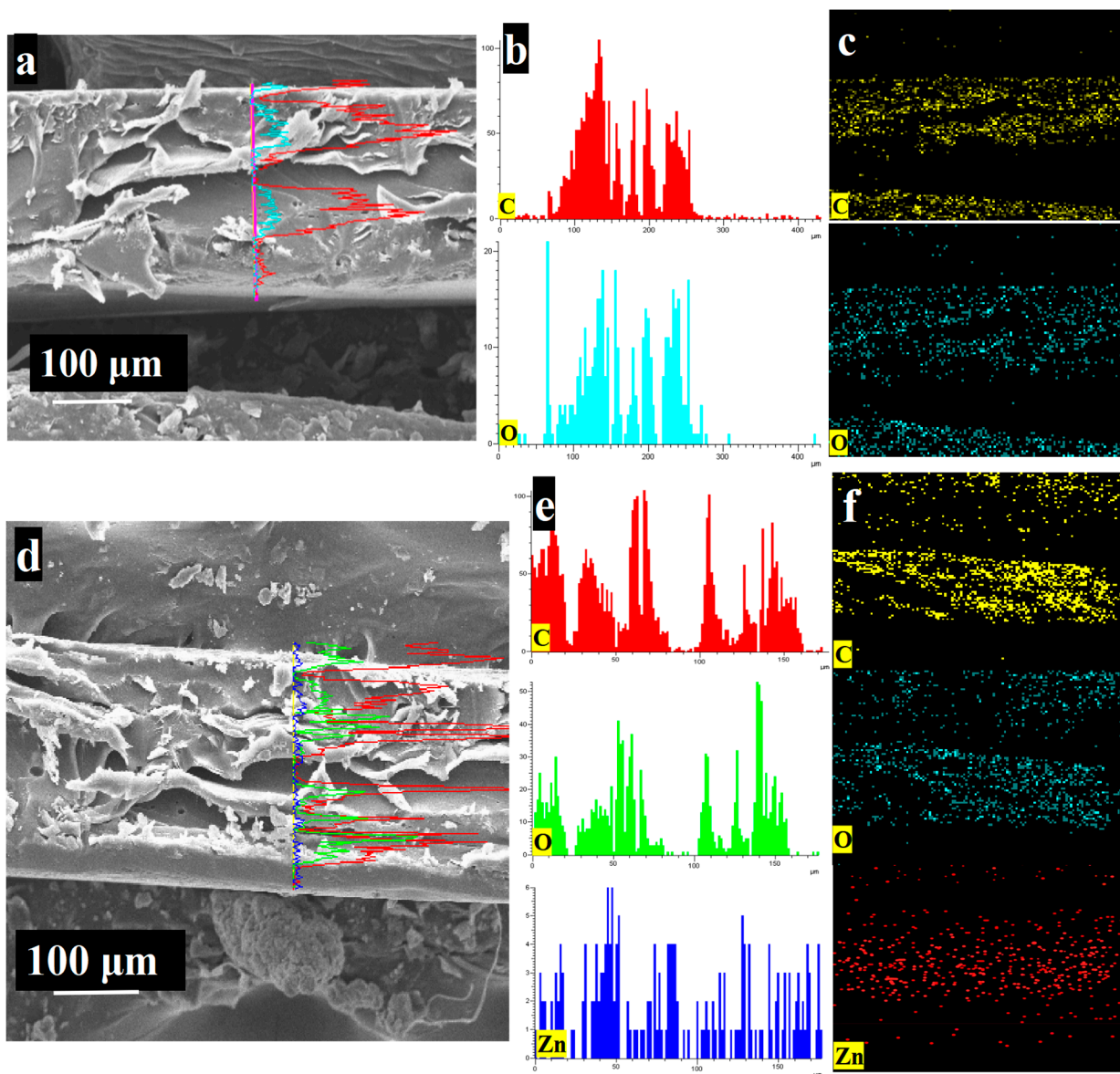


Figure 2. Cont.

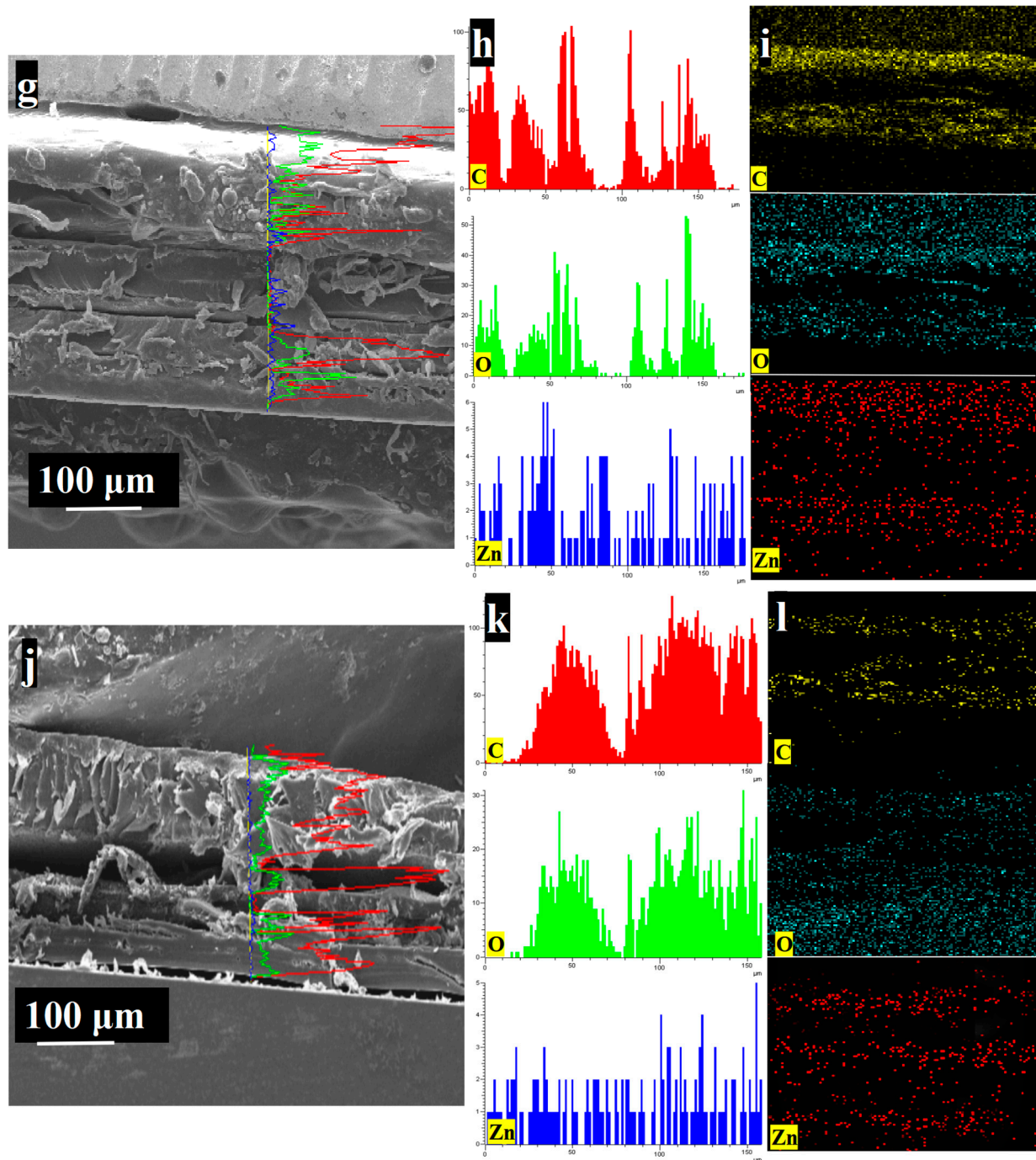


Figure 2. SEM and line-scan mapping images of coating cross sections for (a–c) 4EP, (d–f) 1ZG-4EP, (g–i) 2ZG-4EP, and (j–l) 3ZG-4EP.

3.1.2. Structural Characterization of Samples and Coatings

The FTIR spectra of ZnO–Gr, 4EP and 3ZG-4EP coatings are shown in Figure 3. As shown in Figure 3a, the absorption peaks of the ZnO–Gr samples are located at 1090 cm^{-1} (C–O stretching), 1627 cm^{-1} (Zn–O), and 3415 cm^{-1} (O–H), which indicate that the ZnO nanoparticles are distributed in the interstitial space of graphene layers, and the absorption peak at 453 cm^{-1} is the asymmetric stretching vibration peak of Zn–O bonds [29]. ZnO–Gr includes the characteristic absorption peaks of ZnO and Gr, and the wave number positions of the absorption peaks are unchanged [30,31], which indicates that the functional group structures of both ZnO and Gr remain unchanged, which suggests that ZnO and Gr are physically bound (physisorbed). In the spectra of the 4EP coatings, the characteristic absorp-

tion peak at 3386 cm^{-1} corresponds to the O-H groups on the surface of the coatings, the absorption peak at 2900 cm^{-1} is related to the C-H stretching vibration, and the absorption peak at 1619 cm^{-1} corresponds to the C=C stretching vibration. The peaks in the 4EP coatings that correspond to C-O are at 1030 and 1080 cm^{-1} , respectively. Compared with the original 4EP spectra (Figure 3b,c), a new peak (Zn-O stretching) appears at 1639 cm^{-1} for 3ZG-4EP, which indicates that the ZnO nanoparticles have been successfully doped into Gr and stabilized in the 4EP coatings.

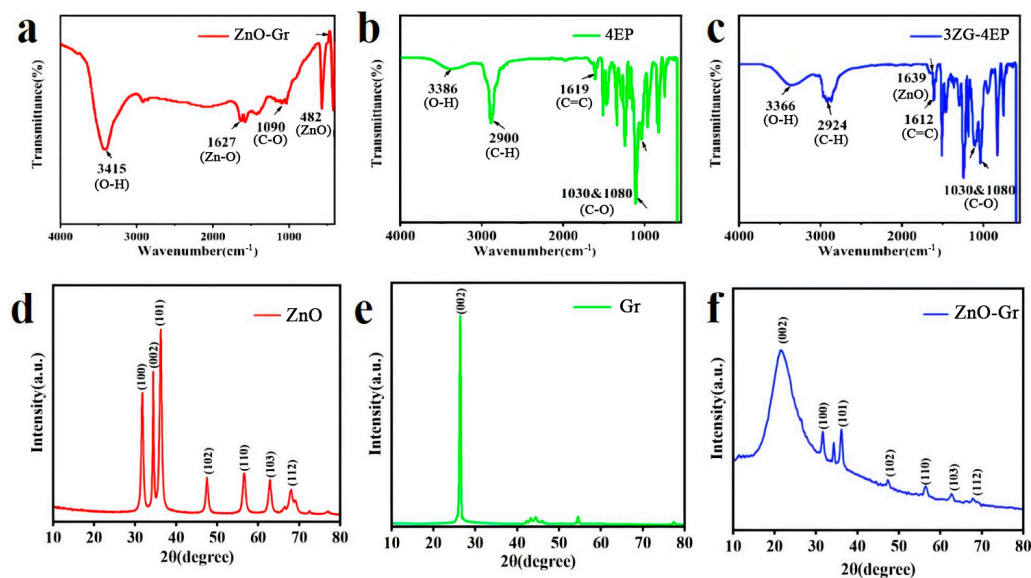


Figure 3. (a) IR spectra of ZnO-Gr; (b) IR spectra of 4EP; (c) IR spectra of 3ZG-4EP; (d) XRD images of ZnO; (e) XRD images of Gr; (f) XRD images of ZnO-Gr.

Figure 3d illustrates the X ray diffraction patterns of zinc oxide, Gr, and ZnO-Gr. The diffraction peaks are found in the three axes (100), (002), (101), (102), (110), (103), (112), (100), (002), (101), (102), (110), (103), and (112). The XRD profile shows that the diffraction peak is 26.3° at 2θ , which is the (002) crystalline surface of graphite with no other peaks. It can be concluded that graphene with high purity was successfully prepared in this experiment [29,30]. In the XRD spectra of ZnO-Gr, there are characteristic diffraction peaks of graphite and nano-ZnO, and the position of the diffraction peaks of the two materials did not change, which proves that the two materials maintained their respective crystalline surfaces after the composite and the ZnO-Gr composite was successfully prepared in this experiment.

3.2. Anticorrosion Properties of XZG-4EP Coatings

3.2.1. Electrochemical Test

The electrochemical impedance spectroscopy (EIS) technique is recognized as one of the most effective methodologies for assessing the corrosion resistance of protective coatings. Consequently, EIS experiments were performed to validate the corrosion resistance properties of the coatings. To synthesize the durable anticorrosive coating XZG-4EP (where $X = 1, 2, 3$), alternating layers of EP and ZnO-Gr dispersions were deposited. To analyze the impact of the shielding effect of the four coatings on the electrochemical impedance test results, the acquired data were fitted using ZView software (ZView 2.8), and the circuit diagram presented in Figure S1 was selected for the fitting process. The EIS spectra are presented in Figure 4, with detailed numerical data provided in Table S1. In the equivalent circuit, R_s represents the solution resistance, while C and R_p denote the constant phase angle element coating capacitance and coating resistance, respectively. The

impedance parameters derived from the fitted circuit are summarized in Table S1. In addition, the values of the dimensionless parameter n are empirical constants. The value of n is $0 \leq n \leq 1$, which is related to the roughness and homogeneity of the coating. When the value of n closes to 1, the constant phase element tends to be pure electricity. On the contrary, the coating approximates pure resistance as the value of n approaches 0. The C value of the coating is intrinsically linked to its shielding efficacy and serves as a critical parameter for assessing the coating's corrosion resistance. A higher porosity in the coating facilitates more rapid water diffusion into the coating's interior, thereby degrading its shielding performance. As water diffuses into the coating matrix, the C value progressively increases, signifying diminished shielding capability. Throughout the entire immersion period, the C value of the XZG-4EP composite coating remained consistently lower than that of the 4EP coating. Despite the gradual increase in the C value due to water diffusion, the water absorption rate of the XZG-4EP composite coating was notably lower compared to the 4EP coating. Conversely, the C value of the 3ZG-4EP composite coating exhibited the lowest values throughout the immersion duration, indicating that both the water absorption and porosity of this coating were inferior to those of the other three coatings. This evidence underscores the superior shielding properties of the 3ZG-4EP composite coating.

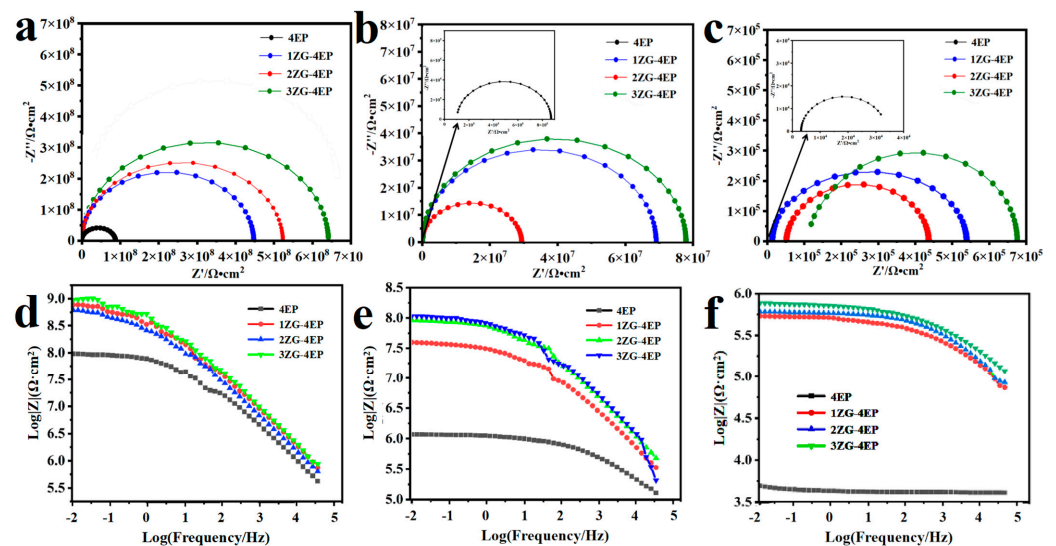


Figure 4. Nyquist plots of the four coatings at different immersion times: (a) 3 days, (b) 1 week, and (c) 2 months. Bode plots of the four coatings at different immersion times: (d) 3 days, (e) 1 week, and (f) 2 months.

The coating resistance (R_p) is a critical parameter that characterizes a coating's ability to resist penetration by corrosive media. A higher coating resistance indicates a stronger penetration resistance, thereby enhancing the coating's shielding and corrosion resistance properties. The corrosion resistance of the coating was evaluated using the data presented in Figure 4a–c and Table S1. 3ZG-4EP showed a maximum electrical resistance value of $7.64 \times 10^8 \Omega \text{ cm}^2$ after three days of immersion in a 3.5 wt.% NaCl solution (Figure 4a), nearly 10 times higher than that of the pure EP ($8.21 \times 10^7 \Omega \text{ cm}^2$), which indicates that the 3ZG-4EP coating has excellent anticorrosion properties. Furthermore, when compared to pure EP coatings, the impedance diameters of 1ZG-4EP and 2ZG-4EP are notably larger, demonstrating that ZnO–Gr can fill in some micro-pores, block the diffusion channel, and enhance the anticorrosive properties of the water-epoxy based paint. This evidence suggests that ZnO–Gr provides the highest resistance to erosion. The resistance profiles of the 3ZG-4EP coatings were similar to those obtained at 3 days of immersion in 3.5 wt.% NaCl (Figure 4b) and 60 days later (Figure 4c). All of the 3ZG-4EP coatings exhibited

the greatest resistance sizes, which were greater than those of 4EP paint, demonstrating that as the amount of ZnO–Gr coats increased, ZnO–Gr dispersed more uniformly in waterborne epoxy resin, and the compound paint had a higher density and could effectively resist penetration of corrosives into the substrate. The coating resistance (R_p) serves as a critical indicator of a coating's ability to resist penetration by corrosive media. A higher coating resistance signifies enhanced penetration resistance, thereby improving the coating's shielding and corrosion resistance properties. As illustrated by the data analysis presented in Figure 4a–c and Table S1, the R_p value generally exhibits a decreasing trend over prolonged immersion time due to electrolyte penetration through the coating's pores. Notably, the R_p value of the 3ZG-4EP composite coating remains consistently the highest throughout the entire immersion period, indicating its superior shielding effect and effective inhibition of corrosive medium penetration, thus enhancing the overall corrosion resistance of the composite coating.

The Bode diagram of all the paint soaked in 3.5 wt% NaCl in Figure 4d–f illustrates the status of the paint in various phases, and it is common for an organic corrosion resistant paint with a high Bode module to have excellent corrosion resistance. The 3ZG-4EP coating, after soaking for three days in 3.5 wt% NaCl (Figure 4d), had a $\log |Z|$ value of $10^9 \Omega \text{ cm}^2$, which was much greater than that of EP paint ($\log |Z| = 10^8 \Omega \text{ cm}^2$), showing that 3ZG-4EP, 1ZG-4EP, and 2ZG-4EP paint all have $\log |Z|$ values of $10^8 \Omega \text{ cm}^2$, which is lower than 3ZG-4EP paint, indicating that penetration of corrosives into the substrate becomes stronger as the number of ZnO–Gr layers increases, and this is consistent with EIS rules. After soaking for seven days in 3.5 wt% NaCl (Figure 4e) and 60 days thereafter (Figure 4f), 3ZG-4EP coatings exhibited the largest resistance diameters. These findings suggest that the density of the composite coatings increases with the addition of ZnO–Gr, thereby enhancing their anticorrosion properties.

To validate the anticorrosive properties of the paint, the Tafel equation was employed to test various coatings. The results are presented in Figure S2, and the details are given in Table S2, where E_{corr} denotes the corrosion potential, i_{corr} signifies the corrosion current density, and $\eta\%$ represents the corrosion inhibition efficiency. The value of $\eta\%$ can be determined using the following formula:

$$\eta = \frac{i_{\text{corr}}^0 - i_{\text{corr}}}{i_{\text{corr}}^0} \times 100\% \quad (1)$$

where i_{corr} represents the corrosion current density of Q235 steel.

Coatings with higher corrosion voltages and smaller corrosion currents have higher corrosion resistance [32–35]. After 60 days of immersion in 3.5 wt% NaCl solution, all the samples containing ZnO–Gr had higher E_{corr} values than 4EP and all the samples containing ZnO–Gr had lower I_{corr} values than 4EP, which indicated that the composite ZnO–Gr coating was more effective in retarding corrosion than the pure 4EP coating. 3ZG-4EP exhibited the largest E_{corr} (-386.6 mV) with the smallest I_{corr} ($8.081 \times 10^{-8} \text{ A cm}^2$), which proved it had the best corrosion protection. The I_{corr} of 3ZG-4EP ($8.081 \times 10^{-8} \text{ A cm}^2$) was almost an order of magnitude lower than that of 1ZG-4EP ($1.366 \times 10^{-7} \text{ A cm}^2$), indicating that ZnO enhances the dispersion of Gr, which reduces the agglomeration of graphene significantly with the increase in the number of layers and fills more microcracks, effectively inhibiting the diffusion of the corrosive medium. Furthermore, the $\eta\%$ efficiencies of 4EP and 3ZG-4EP, as calculated using Formula 1, were 80.12% and 99.14%, respectively. These results are in close agreement with the corresponding EIS test measurements, thus providing robust evidence that 3ZG-4EP demonstrates superior corrosion resistance.

3.2.2. Saltwater Immersion Experiment

To validate the outcomes of the electrochemical tests, four distinct coatings were applied to the Q235 steel plates to assess the corrosion resistance of the substrate under various coatings in a simulated seawater environment, as illustrated in Figure 5. During the initial phase of a one-day immersion test, the surfaces of pure 4EP, 1ZG-4EP, 2ZG-4EP and 3ZG-4EP exhibited smoothness and demonstrated excellent corrosion resistance. After one week of immersion, the cross section of pure 4EP displayed evident signs of corrosion and the coating began to delaminate from the steel substrate. In contrast, the 1ZG-4EP, 2ZG-4EP, and 3ZG-4EP coatings remained unaffected by the corrosive environment. It has been demonstrated that the addition of ZnO-Gr can occupy a limited number of micropores, hinder the diffusion pathway, and improve the corrosion resistance of waterborne epoxy-based coatings. After a two-week immersion period, blistering, cracking, and corrosion were observed at the edges of the 1ZG-4EP coating, whereas the 2ZG-4EP and 3ZG-4EP coatings remained unaffected by the corrosive environment. When the immersion time reached three months, a significant number of rust spots emerged on the edges of both pure 4EP and 1ZG-4EP. In contrast, only minor corrosion was observed on the edges of 2ZG-4EP, while a limited number of air holes formed in the center of its coating. Notably, no rust spots were detected on the 3ZG-4EP coating, and the generation of air holes was virtually negligible. These findings indicate that as the concentration of ZnO-Gr coating increases, the corrosion resistance of the material improves significantly, with 3ZG-4EP demonstrating the highest level of corrosion resistance.

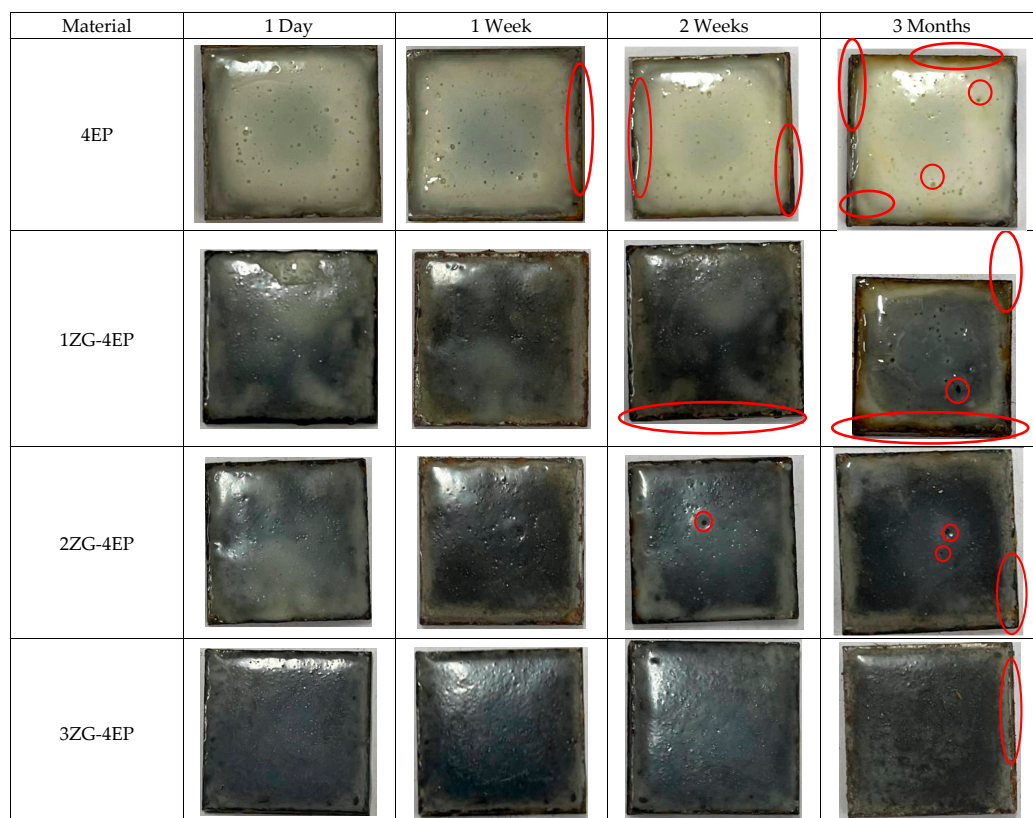


Figure 5. Photographs of four coatings (4EP, 1ZG-4EP, 2ZG-4EP and 3ZG-4EP) immersed in 3.5 wt% NaCl solution for different days of accelerated corrosion tests. Areas circled in red are corrosion pits or rust stains on the surface of the coating.

3.3. Evaluation of Mechanical Durability and Weather Resistance

3.3.1. Mechanical Durability Test

To comprehensively evaluate the wear resistance of 3ZG-4EP coatings, a series of rigorous experiments were conducted. Initially, the coating surface was placed on 1000-grit sandpaper, which is the industry-standard method for simulating everyday wear conditions. Subsequently, a load of 500 g was applied to the coating surface, and the sandpaper was moved approximately 3 cm in the direction illustrated in Figure 6a, ensuring adequate friction was exerted on the surface during each cycle. During the initial phase of the experiment, the contact angle was measured after every five friction cycles to assess changes in the coating's contact angle due to wear. As the experiment progressed, the measurement intervals were incrementally extended, with the contact angle being recorded every 10 cycles to provide a more precise evaluation of the coating's wear stability.

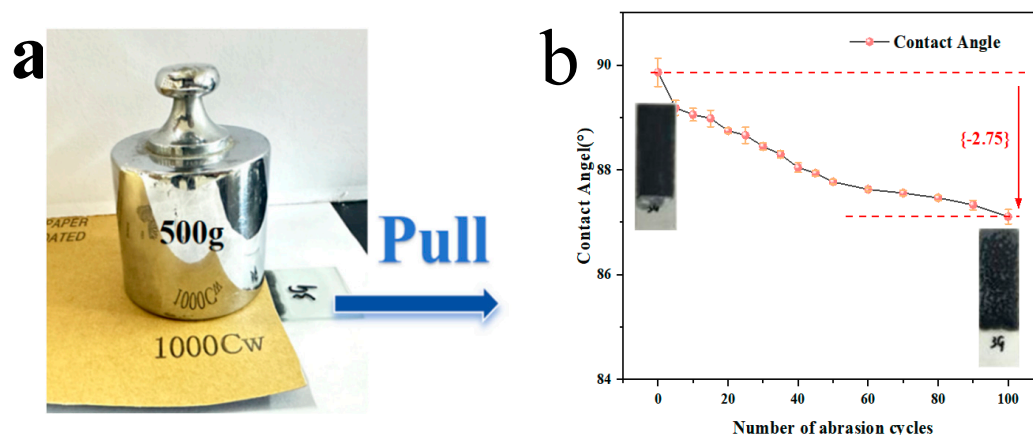


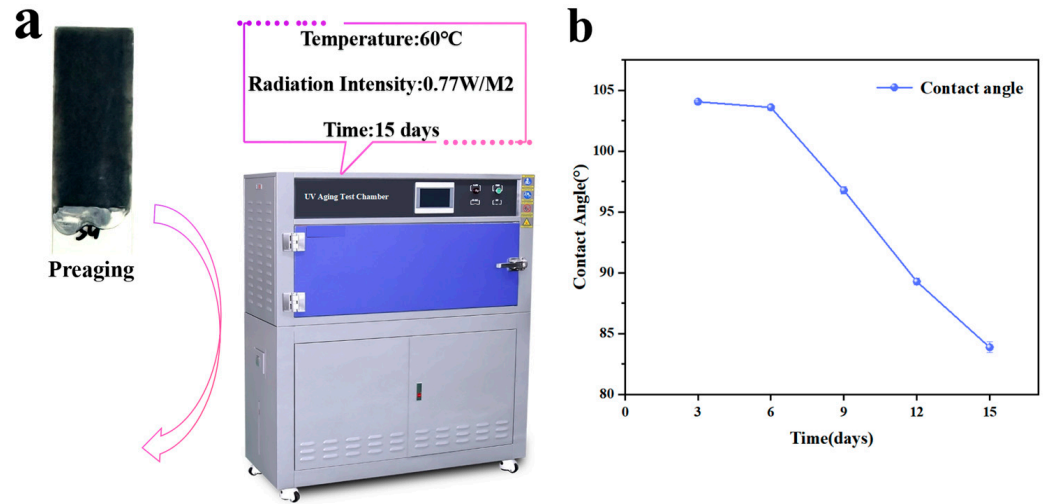
Figure 6. Abrasion resistance of 3ZG-4EP coatings. (a) Friction test of sandpaper on the coated surface. (b) Effect of the number of rubs on the contact angle.

Figure 6b shows the variation in the contact angle of the 3ZG-4EP coating surface with the number of cycles. After the first five rubbing cycles, the contact angle decreased by 1° and then decreased in a linear manner when the number of rubbing cycles was increased to twenty. At 20–40 rubs, the decrease in contact angle decreased, indicating that the coating gradually adapted to the wear and the surface became more stable. Even though the contact angle decreased with increasing friction time, the overall change was not significant. Extensive testing with 100 rubbing cycles showed no significant wear on the coating surface, further demonstrating the excellent mechanical durability of the 3ZG-4EP coatings.

3.3.2. Weather Resistance Test

To study the anti-weathering properties of 3ZG-4EP coatings, a series of strict tests were carried out. Firstly, a uniformly thick super-hydrophobic material was applied to the specimen. The specimens were then put into an ultraviolet curing room and subjected to ultraviolet radiation. To speed the aging process, rapid aging experiments were also carried out at elevated temperatures (60°C), as illustrated in Figure 7a. The purpose of this experiment was to simulate the highest temperatures that a paint can experience in an open space.

Figure 7b shows the effect of UV aging time on the surface of 3ZG-4EP coating. It was found that from 3 to 9 days of UV aging, the contact angle decreased slightly, but did not change much. On the 15th day, the contact angle decreased to 83° due to UV exposure, but no discoloration, chalking, fracture, or flaking was observed. The surface 3ZG-4EP coating has great potential for long-term outdoor use.



After Aging

Figure 7. Aging resistance of 3ZG-4EP coatings. (a) Aging test of coatings. (b) Influence of aging time on contact angle.

3.4. Application Performance of Coating

Figure 8 illustrates the porosity analysis of the coating. The results indicated that the surface porosity of the 4EP coating was 0.96%, and the porosity of 1ZG-4EP, 2ZG-4EP, and 3ZG-4EP decreased to 0.75%, 0.62%, and 0.26%, respectively. Specifically, the surface porosity of the 3ZG-4EP coating was the lowest at 0.26%. These findings suggest that alternating EP and ZnO coatings can effectively fill open pores within the coating, thereby preventing the penetration of corrosive media (such as Cl⁻ and H₂O) into the anticorrosion layer and consequently enhancing the overall corrosion resistance of the coating.

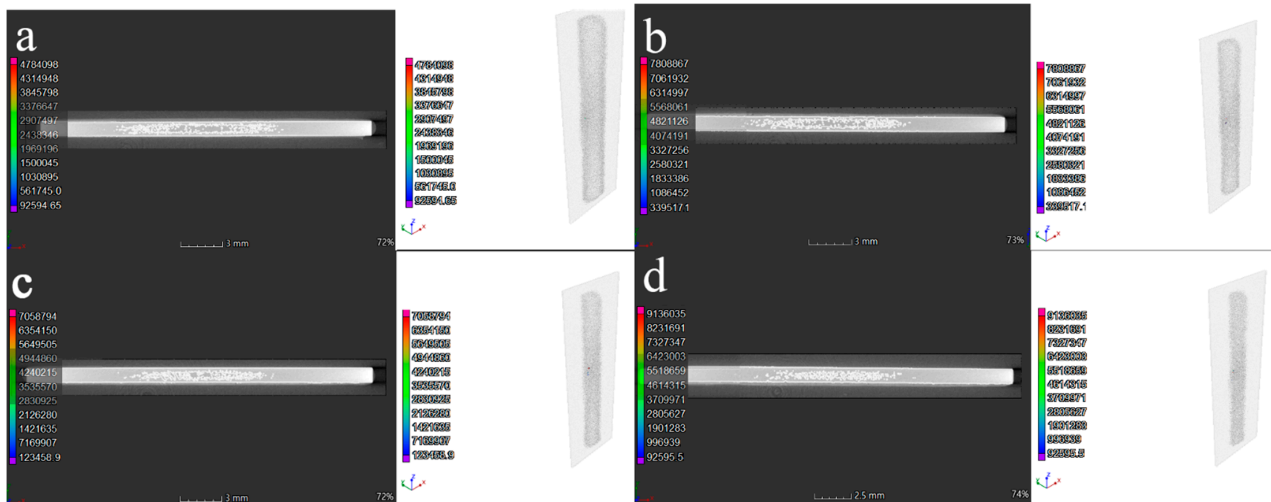


Figure 8. X-CT image of the coating: (a) 4EP; (b) 1ZG-4EP; (c) 2ZG-4EP; (d) 3ZG-4EP.

The adhesion strength of the coating on the steel substrate was assessed using a pull-off adhesion test, with the results presented in Figure S3. The findings indicated that the adhesion strength of the pure epoxy coating was the lowest at 4 ± 0.21 MPa, whereas the adhesion strengths of 1ZG-4EP, 2ZG-4EP, and 3ZG-4EP were 5.3 ± 0.25 MPa, 6.3 ± 0.3 MPa, and 8.2 ± 0.15 MPa, respectively. The adhesion strength of the XZG-4EP composite coating demonstrated a significant enhancement, likely attributable to an increased number of cross-linking points and a higher degree of cross-linking within the system as the number of coated ZnO-Gr sheets increased. This enhancement in intermolecular forces led to a

greater density of hydrogen bonds between the XZG-4EP composite coating and the polar hydroxyl groups of the steel substrate, thereby improving the adhesion of the coating.

As can be seen from Table S3, with the increase in the number of ZnO-Gr layers, the hardness of the obtained coating was significantly increased from H to 3H and the impact resistance is also improved. The results show that the composite coating of ZnO-Gr and EP with a pearl-like structure can form covalent bonds with the epoxy resin, which penetrates the inner part of the nanosheet, and then cross-link the whole coating system to form a strong interfacial bond, which improves the density of the coating and achieves improved barrier and mechanical properties of the coating.

3.5. Corrosion Protection Mechanisms for 4EP and 3ZG-4EP Coatings

In order to reveal the anticorrosion enhancement mechanism of the 3ZG-4EP mimetic coating, corrosion penetration process models of different coating systems were proposed. As shown in Figure 9a, due to the inherent low-barrier property of epoxy resin, during the long-term immersion of pure EP coatings in simulated seawater, the aggressive substances can rapidly penetrate the coating through the defects, such as cracks, pinholes, or scratches, generated during the coating preparation and curing process, and undergo large-scale diffusion to make the coating fail rapidly, leading to the corrosion of the carbon steel substrate [36]. In this experiment, inspired by the ordered arrangement of the interfacial structure of shell pearl layers, a shell-like bionic coating (XZG-4EP ($X = 1, 2, 3$)) coated with ZnO-Gr alternately with EP was prepared to improve the dispersibility of graphene by ZnO doping graphene and to reduce the defects of the coating micropores due to the agglomeration of graphene. In addition, the introduction of graphene flakes formed a “labyrinth” structure, which increased the tortuosity of the diffusion path of aggressive substances and thus effectively enhanced the barrier properties of the XZG-4EP ($X = 1, 2, 3$) coatings, which in turn improved the anticorrosive properties of the coatings. In summary, the main protective mechanism of the 3ZG-4EP coating (Figure 9b) can be summarized as follows: (1) the strong interfacial bond between the ZnO-Gr layer and the EP coating and the continuous layer structure increase the denseness of the coating system [37]; and (2) the dense ZnO-Gr layer in the biomimetic structure comprises numerous graphene sheets assembled in parallel. This configuration generates a multitude of tortuous corrosion pathways, significantly hindering the penetration of corrosive agents. Consequently, this arrangement effectively extends the time required for corrosive media to reach the interior of the coating, thereby enhancing the coating’s durability.

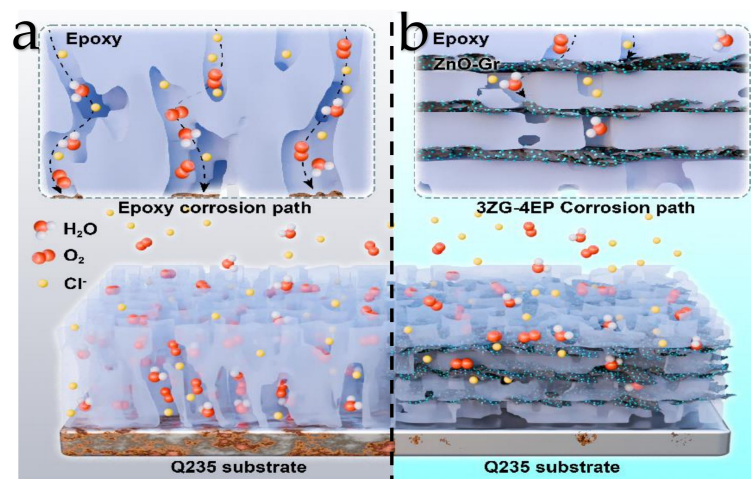


Figure 9. Corrosion protection mechanisms for coatings: (a) 4EP; (b) 3ZG-4EP.

4. Conclusions

In this study, graphene and zinc oxide were co-assembled and incorporated into an epoxy resin matrix. Shell-like biomimetic composite coatings (XZG-4EP, where X = 1, 2, 3) were subsequently fabricated through the alternating deposition of ZnO-Gr layers and epoxy resin in varying numbers of layers. The ZnO-Gr nano-compound can be used as a protective material to protect the corrosion electrolyte from penetrating into the paint. The uniform dispersion of ZnO-Gr sheets can reduce the flaws in the micro-holes and create a powerful blocking action, while the ZnO-Gr sheet is introduced into the coating, creating a “maze” structure within the coating, which makes the diffusion path of the invasive material more curved, thereby improving the anticorrosion property of the paint efficiently. The anticorrosion property of the paint improved as the ZnO-Gr amount was increased, the corrosive potential rose from -567.075 mV to -386.6 mV, and the corrosion current decreased from 1.366×10^{-7} A cm² to 8.081×10^{-8} A cm². After immersing the different composite coatings in NaCl solution for two months, the corrosion resistance of 3ZG-4EP (5.55×10^6 Ω cm²) still had the largest impedance arc compared to 4EP (4.40×10^4 Ω cm²), 1ZG-4EP (4.01×10^5 Ω cm²), and 2ZG-4EP (4.79×10^5 Ω cm²). The values of impedance modulus ($f = 0.01$ Hz) of 3ZG-4EP were found to be higher at three days (10^9 Ω cm²), one week (10^8 Ω cm²), and two months (10^6 Ω cm²), showing the highest Bode modulus values and indicating better interfacial interactions of 3ZG-4EP. As a barrier layer enhancer, zinc oxide improves the dispersion of graphene, resulting in a more homogeneous and proportional dispersion of graphene, and the shell-like structure of the 3ZG-4EP bionic coatings has shown potential as an anticorrosive coating.

Supplementary Materials: The following supporting information can be downloaded at <https://www.mdpi.com/article/10.3390/coatings15010063/s1>, Figure S1: Equivalent electrical circuit; Table S1: Electrochemical parameters extracted from EIS experiment for 4EP, 1ZG-4EP, 2ZG-4EP and 3ZG-4EP electrode immersed in a 3.5 wt% NaCl aqueous solution; Figure S2: Tafel polarization curves of 4EP, 1ZG-4EP, 2ZG-4EP, and 3ZG-4EP coatings at 60 days; Table S2: The value of corrosion potential, corrosion current and corrosion inhibition rate for Q235, 4EP, 1ZG-4EP, 2ZG-4EP and 3ZG-4EP coatings in Tafel image; Table S3: Numerical coating thickness, adhesion test, hardness test and impact resistance test results; Figure S3: The results of the pull-off adhesion test for the 4EP, 1ZG-4EP, 2ZG-4EP, and 3ZG-4EP coatings.

Author Contributions: Conceptualization, Y.W. and L.M.; methods, Y.N. and H.M.; formal analysis, L.M., Y.L. and K.L.; research, Y.N. and H.M.; writing—initial draft, Y.W. All authors have read and agreed to the published version of the manuscript.

Funding: The authors acknowledge that this work has been supported by the Young Elite Scientists Sponsorship Program by CAST (2022QNRC001), the Scientific Research Division of Heilong Jiang Province (LH2022B022), Jiamusi University National Fund Incubation Program (JMSUGPZR2023-006), the North Unique Medicine Research and Development Team (DJXSTD202403), Jiamusi University and the East Pole Team (DJXSTD202403).

Institutional Review Board Statement: Not applicable.

Informed Consent Statement: Not applicable.

Data Availability Statement: This paper and the Supplementary Materials include the information.

Conflicts of Interest: Author Kuilin Lv was employed by the company China Testing & Certification International Group Co., Ltd. The remaining authors declare that the research was conducted in the absence of any commercial or financial relationships that could be construed as a potential conflict of interest.

References

1. Jing, Y.; Wang, P.; Yang, Q.; He, Y.; Bai, Y. Molybdenum disulfide with poly(dopamine) and epoxy groups as an efficiently anticorrosive reinforcers in epoxy coating. *Synth. Met.* **2020**, *259*, 116249. [\[CrossRef\]](#)
2. Kumari, S.; Mungse, H.P.; Gusain, R.; Kumar, N.; Sugimura, H.; Khatri, O.P. Octadecanethiol-grafted molybdenum disulfide nanosheets as oil-dispersible additive for reduction of friction and wear. *FlatChem* **2017**, *3*, 16–25. [\[CrossRef\]](#)
3. Bagherzadeh, M.; Mahdavi, F.; Ghasemi, M.; Shariatpanahi, H.; Faridi, H. Using nanoemeraldine salt-polyaniline for preparation of a new anticorrosive water-based epoxy coating. *Prog. Org. Coat.* **2010**, *68*, 319–322. [\[CrossRef\]](#)
4. Xiao, H.; Liu, S. Zirconium phosphate (ZrP)-based functional materials: Synthesis, properties and applications. *Mater. Des.* **2018**, *155*, 19–35. [\[CrossRef\]](#)
5. Pica, M. Zirconium Phosphate Catalysts in the XXI Century: State of the Art from 2010 to Date. *Catalysts* **2017**, *7*, 190. [\[CrossRef\]](#)
6. BAHmed, B.; Anjum, D.H.; Gogotsi, Y.; Alshareef, H.N. Atomic layer deposition of SnO₂ on MXene for Li-ion battery anodes. *Nano Energy* **2017**, *34*, 249–256.
7. Ma, I.A.W.; Sh, A.; Ramesh, K.; Vengadaesvaran, B.; Ramesh, S.; Arof, A.K. Anticorrosion properties of epoxy-nanochitosan nanocomposite coating. *Prog. Org. Coat.* **2017**, *113*, 74–81.
8. Hu, Y.; Wang, Y.; Zeng, Z.; Zhao, H.; Ge, X.; Wang, K.; Wang, L.; Xue, Q. PEGlated graphene as nanoadditive for enhancing the tribological properties of water-based lubricant. *Carbon* **2018**, *137*, 41–48. [\[CrossRef\]](#)
9. Yu, Y.-H.; Lin, Y.-Y.; Lin, C.-H.; Chan, C.-C.; Huang, Y.-C. High-performance polystyrene/graphene-based nanocomposites with excellent anticorrosion properties. *Polym. Chem.* **2013**, *5*, 535–550. [\[CrossRef\]](#)
10. Sun, W.; Wu, T.; Wang, L.; Yang, Z.; Zhu, T.; Dong, C.; Liu, G. The role of graphene loading on the corrosion-promotion activity of graphene/epoxy nanocomposite coatings. *Compos. Part B* **2019**, *173*, 106916. [\[CrossRef\]](#)
11. Ren, S.; Cui, M.; Li, W.; Pu, J.; Xue, Q.; Wang, L. N-doping of graphene: Toward long-term corrosion protection of Cu. *J. Mater. Chem. A* **2018**, *6*, 24136–24148. [\[CrossRef\]](#)
12. Shtein, M.; Nadiv, R.; Buzaglo, M.; Kahil, K.; Regev, O. Thermally conductive graphenepolymer composites: Size, percolation, and synergy effects. *Chem. Mater.* **2015**, *27*, 2100. [\[CrossRef\]](#)
13. Wang, J.; Du, P.; Ding, J.; Pu, J.; Xie, B. Graphene oxide enhanced aqueous epoxy composite coating derived from sustainable cardanol resource for corrosion protection. *Surf. Topogr. Metrol. Prop.* **2019**, *7*, 044002. [\[CrossRef\]](#)
14. Ding, R.; Chen, S.; Zhou, N.; Zheng, Y.; Li, B.-J.; Gui, T.-J.; Wang, X.; Li, W.-H.; Yu, H.-B.; Tian, H.-W. The diffusion-dynamical and electrochemical effect mechanism of oriented magnetic graphene on zinc-rich coatings and the electrostatics and quantum mechanics mechanism of electron conduction in graphene zinc-rich coatings. *J. Alloys Compd.* **2019**, *784*, 756–768. [\[CrossRef\]](#)
15. Zhang, Y.; Tian, J.; Zhong, J.; Shi, X. Thin nacre-biomimetic coating with superanticorrosion performance. *ACS Nano* **2018**, *12*, 10189–10200. [\[CrossRef\]](#)
16. Um, J.G.; Habibpour, S.; Jun, Y.S.; Elkamel, A.; Yu, A. Development of π - π interaction-induced functionalized graphene oxide on mechanical and anticorrosive properties of reinforced polyurethane composites. *Ind. Eng. Chem. Res.* **2020**, *59*, 3617–3628. [\[CrossRef\]](#)
17. Lv, K.; Wan, D.; Pan, R.; Suo, W.; Zhu, Y. Curvature of NCNTs induced selectivity of CO₂ electroreduction into CO. *Carbon Neutralization* **2022**, *1*, 189–197. [\[CrossRef\]](#)
18. Du, P.; Qiu, S.; Liu, C.; Liu, G.; Zhao, H.; Wang, L. In situ polymerization of sulfonated polyaniline in layered double hydroxide host matrix for corrosion protection. *New J. Chem.* **2018**, *42*, 4201–4209. [\[CrossRef\]](#)
19. Lu, X.; Liu, L.; Xie, X.; Cui, Y.; Oguzie, E.E.; Wang, F. Synergetic effect of graphene and Co(OH)₂ as cocatalysts of TiO₂ nanotubes for enhanced photogenerated cathodic protection. *J. Mater. Sci. Technol.* **2020**, *37*, 55–63. [\[CrossRef\]](#)
20. Jing, Y.; Wang, P.; Yang, Q.; Wang, Q.; Bai, Y. MoS₂ decorated with ZrO₂ nanoparticles through mussel-inspired chemistry of dopamine for reinforcing anticorrosion of epoxy coatings. *Colloids Surf. A Physicochem. Eng. Asp.* **2021**, *608*, 125625. [\[CrossRef\]](#)
21. Ding, J.; Zhao, H.; Yu, H. Bioinspired strategies for making superior graphene composite coatings. *Chem. Eng. J.* **2022**, *435*, 134808. [\[CrossRef\]](#)
22. Li, Z.Y.; Cai, Z.B.; Zhou, T.; Cui, X.J.; Zhu, M.H. New Impact Resistance Bionic Composite Coating Inspired by Turtle Shell. *J. Mater. Eng. Perform.* **2023**, *32*, 334–347. [\[CrossRef\]](#)
23. Jiheng, D.; Hongran, Z.; Yu, H. Bio-inspired Multifunctional Graphene-Epoxy Anticorrosion Coatings by Low-Defect Engineered Graphene. *ACS Nano* **2022**, *16*, 710–720.
24. Wegst, U.G.K.; Bai, H.; Saiz, E.; Tomsia, A.P.; Ritchie, R.O. Bioinspired structural materials. *Nat. Mater.* **2015**, *14*, 23–36. [\[CrossRef\]](#)
25. Askarinejad, S.; Rahbar, N. Toughening mechanisms in bioinspired multilayered materials. *J. R. Soc. Interface* **2015**, *12*, 20140855. [\[CrossRef\]](#)
26. Barthelat, F.; Tang, H.; Zavattieri, P.D.; Li, C.-M.; Espinosa, H.D. On the mechanics of mother-of-pearl: A key feature in the material hierarchical structure. *J. Mech. Phys. Solids* **2007**, *55*, 306–337. [\[CrossRef\]](#)
27. Munch, E.; Launey, M.E.; Alsem, D.H.; Saiz, E.; Tomsia, A.P.; Ritchie, R.O. Tough, bio-inspired hybrid materials. *Science* **2008**, *322*, 1516–1520. [\[CrossRef\]](#)

28. Dea, S.; Lutkenhaus, J.L. Corrosion behaviour of eco-friendly airbrushed reduced graphene oxide-poly(vinyl alcohol) coatings. *Green Chem.* **2018**, *20*, 506–514. [[CrossRef](#)]
29. Ding, J.; Zhao, H.; Yu, H. Superior to graphene: Super-anticorrosive natural mica nanosheets. *Nanoscale* **2020**, *12*, 16253–16261. [[CrossRef](#)] [[PubMed](#)]
30. Dusza, M.; Granek, F.; Streck, W. Illumination intensity dependent photoresponse of ultra-thin ZnO/graphene/ZnO heterostructure. *Opt. Mater.* **2017**, *74*, 176–182. [[CrossRef](#)]
31. Lu, Y.-M.; Tseng, C.-F.; Lan, B.-Y.; Hsieh, C.-F. Fabrication of Graphene/Zinc Oxide Nano-Heterostructure for Hydrogen Sensing. *Materials* **2021**, *14*, 6943. [[CrossRef](#)] [[PubMed](#)]
32. Lv, K.; Bao, Y.; Ma, H.; Liu, X.; Zhu, Y.; Wan, D. Size Effect of Graphite Nanosheet-Induced Anti-Corrosion of Hydrophobic Epoxy Coatings. *Coatings* **2024**, *14*, 769. [[CrossRef](#)]
33. Ma, H.; Zhang, X.; Liu, X.; Wan, D.; Lv, K. Controllable size of graphite nanosheets and functionalized SiO₂ microspheres with excellent anti-corrosive/wear function for superhydrophobic coating. *Mater. Today Commun.* **2024**, *40*, 110026. [[CrossRef](#)]
34. Yang, Z.; Che, J.; Zhang, Z.; Yu, L.; Hu, M.; Sun, W.; Cao, W.; Fan, J.; Wang, L.; Liu, G. High-efficiency graphene/epoxy composite coatings with outstanding thermal conductive and anti-corrosion performance. *Compos. Part A* **2024**, *181*, 108152. [[CrossRef](#)]
35. Wei, R.; Liu, Z.; Wei, W.; Wang, S.; Lv, Y.J.; Han, G.C. Anticorrosion performance of hydrophobic acid-modified-MOFs/epoxy coatings. *Colloid Interface Sci. Commun.* **2022**, *46*, 100580. [[CrossRef](#)]
36. Qiu, S.; Su, Y.; Zhao, H.; Wang, L.; Xue, Q. Ultrathin metal-organic framework nanosheets prepared via surfactant-assisted method and exhibition of enhanced anticorrosion for composite coatings. *Corros. Sci.* **2021**, *178*, 109090. [[CrossRef](#)]
37. Zhao, H.; Ding, J.; Yu, H. Advanced bio-based UV-curable anticorrosive coatings reinforced by hBN. *ChemistrySelect* **2018**, *3*, 1–8. [[CrossRef](#)]

Disclaimer/Publisher's Note: The statements, opinions and data contained in all publications are solely those of the individual author(s) and contributor(s) and not of MDPI and/or the editor(s). MDPI and/or the editor(s) disclaim responsibility for any injury to people or property resulting from any ideas, methods, instructions or products referred to in the content.